

# Age of Information-based Performance of Ultrasonic Communication Channels for Nanosensor-to-Gateway Communication

Jorge Torres Gómez, *Senior Member, IEEE*, Joana Angjo, and Falko Dressler, *Fellow, IEEE*

**Abstract**—The successful connection between in-body nanosensors and gateway devices outside the human body enables the identification of diseases, before symptoms even appear. In this paper, we investigate the timely detection of abnormalities using nanosensors flowing in the blood vessels and reporting to external wearable devices. We develop analytic solutions to evaluate the information freshness using the average peak age of information (PAoI) metric. We model the mobility of nanosensors in the blood flow as a random process through a Markov chain. The communication capabilities with external devices to report detected abnormalities are modeled as a linear time-variant (LTV) channel. Besides, for communication with external devices, we study the impact of the mobility of nanosensors when using ultrasonic waveforms and integrate it with the PAoI formulation. In addition to a previously proposed analytical model, we perform large-scale simulations using Blood Voyager Simulator (BVS) and the network simulator ns-3. As primary metrics, we use the bit error rate (BER), the packet error rate (PER), and the average PAoI. The results give clear insights into the impact of the position of the external monitor. We also illustrate that local communication performance almost does not influence the average PAoI.

**Index Terms**—In-body nanocommunication, ultrasonic, blood vessels, mobility, Markov model, ns-3, age of information (AoI)

## I. INTRODUCTION

Nanocommunication technologies have propelled to the forefront of future processes for diagnosis and treatment in precision medicine [1]–[3]. The capability of nanocommunication to provide non-invasive solutions and reach delicate locations of the human body while early reporting are some of the reasons behind its potential [4]. Nanosensors injected in the human circulatory system (HCS) can be utilized to monitor the internal functions of the organism and report results to an external monitor outside of the body [3], [5].

We consider an application scenario in precision medicine where nanosensors survey the human body to identify potential abnormalities, as depicted in Fig. 1. The nanosensors are traveling within the blood vessels (cf. Fig. 1 b) of the HCS (cf. Fig. 1 a), and they have sensing capabilities for detecting the molecules released during quorum sensing (QS) communications among the bacteria (as the abnormality).

Reported research was supported in part by the project MAMOKO funded by the German Federal Ministry of Education and Research (BMBF) under grant number 16KIS0917 and by the project NaBoCom funded by the German Research Foundation (DFG) under grant number DR 639/21-1

J. Torres Gómez, J. Angjo, and F. Dressler are with the School of Electrical Engineering and Computer Science, TU Berlin, Berlin, Germany, Email: {torres-gomez, angjo, dressler}@ccs-labs.org

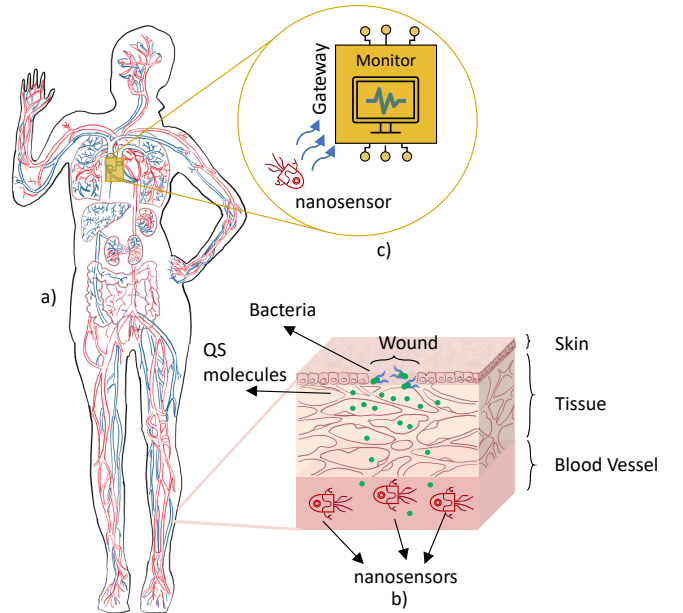


Fig. 1: In-vivo disease detection scheme. a) Human circulatory system. b) Molecular communications for disease detection. c) Communication between nanosensors and the external monitor.

The information detected by the nanosensors will then be communicated to the monitor (cf. Fig. 1 c) once they travel to the right heart chamber, on top of which the monitor is positioned. The successful report of their sensing data to the monitor is directly related to the quality of the communication link between the in-body network to the body area network, which is challenging due to the heterogeneous channel between them. Besides, the timely data report will depend on the random nature of the nanosensors' traveling path along the HCS.

To enable the communication link between nanosensors and the external gateway, we follow our previous work in [6] using ultrasonic communication channels. Compared to electromagnetic waves, ultrasound waves experience less absorption within the human body, which mainly consists of water [7]. As supported by measurements, ultrasonic communication in human tissues exhibits a similar gain as in water, thus, making it a preferable solution for health-related applications [8]–[11]. Investigation of the propagation of ultrasonic waveforms has been accomplished by using very small transducers and reported to evaluate propagation delay, excess delay, and channel impulse response (CIR) [7], [8], [12].

This research extends the results presented in [6] by aiming to evaluate further the overall detection performance using the average peak age of information (PAoI) metric. We assess the average PAoI metric as integrating the ultrasonic communication performance. Given the fact that reliability and real-time data reporting capabilities are critical in healthcare applications, the average PAoI is a useful metric to estimate the freshness of the status update about potential abnormalities [13]. We evaluate the average PAoI integrating the random path of nanosensors along the HCS [14] and their communication errors in the interface with the external gateway [6].

The results obtained from the simulations and analytical modeling are further verified by implementing the intrabody communication link in the Blood Voyager Simulator (BVS) platform [15]. The model is again built upon experimental data for signal gain and bit error rate (BER) as published in [7].

Our main contributions can be summarized as follows:

- We assess the performance of ultrasonic communication channels for in-body nanocommunication;
- we perform simulations to evaluate the impact of nanosensors' mobility using the network simulator ns-3; and
- we model and evaluate the PAoI metric for ultrasound communications upon a Markov chain representation.

The rest of the paper is structured as follows. We summarize related work in Section II aiming to provide further details on this research context. We introduce the system model in Section III focusing on the nanosensor mobility from large and small-scale perspectives. We model the ultrasonic linear time-variant (LTV) channel in Section IV including its implementation in the simulator BVS. We integrate the mobility model and the nanosensor-gateway link performance within the average PAoI formulation in Section V. Finally, we discuss our findings in Section VI and conclude the paper in Section VII.

## II. RELATED WORK

Conventional radio frequency electromagnetic waves are not an optimal solution for in-body networks, as they experience high attenuation when propagating through human tissue. Additionally, low-power consumption is a constraint, not only for elongating the operation time of the devices but also for preventing them from heating. Molecular communication (MC) is another solution proposed in the literature, which mainly focuses on enabling the communication of the nanosensors between each other within the HCS [16]–[18]. Although not suitable for the communication of the nanosensors with the gateway, MC is an energy-efficient solution, in which the nanosensors establish communication through signals carried by molecule particles. Another enabling technology discussed for in-body to body area networks is terahertz communication [19]–[21]. However, this technology has its own challenges, such as dominant shadowing and limited communication distances within the body.

Following up on the advantages of ultrasonic communications various research focus on the achievable performance. From the communication perspective, the received signal is affected by multiple parameters, such as propagation speed and channel gain. The sound *propagation speed* in human tissues

is stated to be in the range of 1450–1540 m/s in [7]–[9]; unlike in [11], where it is assumed to be in the range of 330–3600 m/s, considering not only tissue but for example gas and air bubbles in the lungs. This means that the results are dependent on the setups and testbeds considered in different studies.

The attenuation level that the received signal experiences varies with the *frequency* used, as well as the tissue where the communication takes place. The frequency and *distance* have a crucial effect on the received signal. In medical diagnostics, the used frequencies are usually in the 2–10 MHz range. For example, the authors of Santagati et al. [22] use frequencies up to 10 MHz and experience an acceptable gain based on a mathematical model. On the other hand, Bos et al. [7] consider 1.19 MHz to be the best frequency for distances of several centimeters based on a testbed. In our previous work [6], we analyzed the effect of different utilized frequencies on the performance of ultrasonic communication channels, including a practical case with mobility in the vessels. The results showed that the signal to noise ratio (SNR) value can drop from 15 dB to –40 dB in less than 5 ms for different frequencies.

The results provided by Bos et al. [7] and Sciacca and Galluccio [8] build a solid foundation for the characterization of ultrasonic in-body communication channels. The *channel impulse response* contributed by Bos et al. [7] is of particular interest, since the received signal can be obtained by simple convolution of the transmitted signal. In [7], the human tissue is mimicked through the usage of gelatin phantoms, which are submersed into an anechoic water tank for representing the implanted transducers. The transmitter and receiver are then attached at the ends of a phantom at three different communication distances, namely 2 cm, 4 cm, and 8 cm, for which the CIR is measured accordingly. A waveform generator is used to produce a pulse for transmission, whereas the reception and the measurement of the amplitude of the received signal are done by using the oscilloscope. Sciacca and Galluccio [8] and Galluccio et al. [9] considered 5.5 cm, 10 cm, and 12 cm distances between transmitter and receiver. The CIR is modeled with a low pass filter and coefficients are estimated through fitting techniques [7], [8].

The applications of in-body communication networks emphasize the importance of the constraints on reliability and latency. As mentioned above, the age of information (AoI) metrics can provide valuable insight for evaluating the system's performance in terms of how fresh the received information at the monitor is. The concept of average AoI and PAoI of in-body communication networks were first introduced and analyzed in [23]. The AoI concept was integrated within the BVS simulation framework and the freshness of the status update packets is investigated for three different locations: the brain, the liver, and the kidney. The results show that AoI is directly related to the number of injected nanosensors, the status update interval and the visiting probability of nanosensors to a specific location of the human body. This metric can be very valuable in further enhancing the system by optimizing, e.g., the number of nanosensors, the gateway position, and the sensor storage capabilities.



on the skin's surface. When the nanosensor flows near the monitor, it can communicate with the monitor device with packet emissions. The longest communication distance between the nanosensor and the monitor corresponds to the distance between them at time  $t_{in}$  and  $t_{out}$ , whereas the shortest corresponds to the distance between them at time  $t_{below}$  in Fig. 3.

Fig. 4 illustrates the minimum and maximum communication distances between the devices in more detail. The minimum communication distance between the monitor and the nanosensor is denoted by  $l_v$ . This value might result in smaller than the summation of the skin, fat and blood thicknesses (denoted by  $L_s$ ,  $L_t$ , and  $L_v$ , respectively), since the nanosensor may be moving in different bloodstreams. These distances vary for different tissues in the human body, and their values are obtained as indicated in [29], [30]. The angle depicted as  $\varphi$  denotes the angle between the shortest and the largest communication distances. In other words, the nanosensor in Fig. 4 can communicate with the monitor throughout a total distance of  $2 \times x_{max}$ .

#### IV. MODELING IN-BODY COMMUNICATION PERFORMANCE

In this section, we provide details on the communication model between the nanosensors and the gateway. We also provide details on the communication model implementation in the BVS simulator.

##### A. Fundamentals

Taking into account the movement of the nanosensor (cf. Fig. 5), the communication performance between the two devices is modeled by a LTV channel. Also, it includes the Doppler effect for ultrasound communications. Since the distance between the nanosensor and the monitor changes with time, the channel gain and delay are time-dependent. The variables  $t_i$  highlight certain points in time during the movement process of a nanosensor (see Fig. 4). Timepoint  $t_{in}$  marks the time the nanosensor gets into the communication range of the monitor. Timepoint  $t_{below}$  marks the situation when the nanosensor is directly below the monitor and the angle of reception  $\phi_{t_2}$  is, therefore,  $\frac{\pi}{2}$ . For every time instant  $t_i$ , there is a combination of  $(h_{t_i}, \tau_{t_i})$ , where  $h_{t_i}$  describes the channel impulse response and  $\tau_{t_i}$  describes the propagation delay for the current point in time.

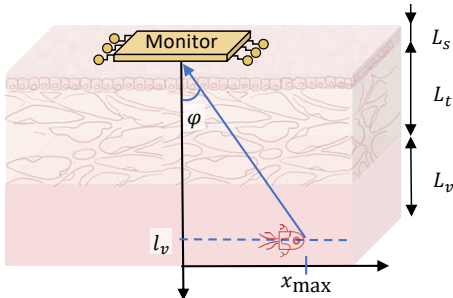


Fig. 4: Conceptual representation of the communication range between the monitor and the moving nanosensors.

To describe the impact of the LTV channel on the received signal  $r(t)$  (ultrasonic waveform), we use the formula provided in [31] as

$$r(t) = g_d s(t - \tau_d) e^{j2\pi\nu t}, \quad (1)$$

where  $s(t)$ ,  $g_d$ ,  $\tau_d$ , and  $\nu$  represent the transmitted signal, gain factor, delay, and Doppler frequency corresponding to the given distance between the nanosensor and the monitor here denoted as  $d$ .

The Doppler frequency can be obtained as

$$\nu = v \cos(\phi) \frac{f_c}{c_u}, \quad (2)$$

where  $v$  is the velocity of the nanosensor,  $c_u$  is the propagation speed of the ultrasonic waveform,  $f_c$  is the carrier frequency, and  $\phi$  is the angle of arrival of the wave relative to the direction of motion of the nanosensor, as depicted in Fig. 5. For the in-body scenario, we consider typical velocities  $v$  of the nanosensor in the human circulatory system in the aorta ( $v = 0.2$  m/s), arteries ( $v = 0.1$  m/s), and veins ( $v = 0.03$  m/s) [28].

According to Eq. (1), the impact of the LTV channel can be analyzed through the three different terms  $g_d$ ,  $\tau_d$ , and  $\nu$ . The terms  $g_d$  and  $\tau_d$  can be directly computed based on the distance between the nanosensor and the monitor. In contrast, the  $\nu$  term is dependent on the dynamic of movement according to the path trajectory and the velocity ( $\phi$  and  $v$  in Eq. (1)), as well as the communication parameters given by the center frequency  $f_c$  and the signal propagation speed  $c_u$  in Eq. (2).

We evaluate the three terms  $g_d$ ,  $\tau_d$ , and  $\nu$  in Eq. (1), assuming that a nanosensor moves on a linear path trajectory from left to right, as depicted in Fig. 5. This results in a valid approximation for the traveling path of nanosensors, as they are driven through the laminar blood flow in the vessels [28]. To compute the gain and delay, we use the curve fitting method provided by Matlab for the results of the measurements given by [7],<sup>1</sup> where the

<sup>1</sup>Published by Thomas Bos under the CC-BY-SA 4.0 license on GitHub <https://github.com/BosThomas/USbodyComm>

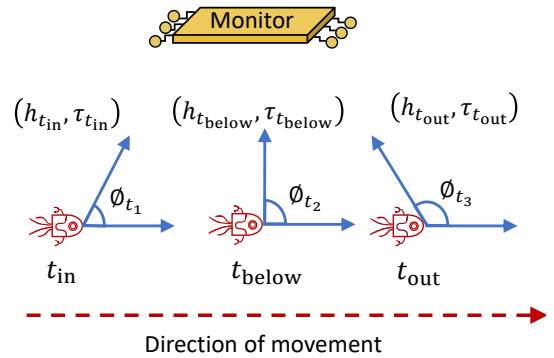


Fig. 5: System model for ultrasound communication from in-body nanosensors to a gateway system. The flowing nanosensor navigates through a given blood vessel. Depicted are the relevant communication link properties at time steps  $t_{in}$  (nanosensor gets into communication range with the monitor),  $t_{below}$  (nanosensor is closest to the monitor), and  $t_{out}$  (nanosensor leaves the communication range).

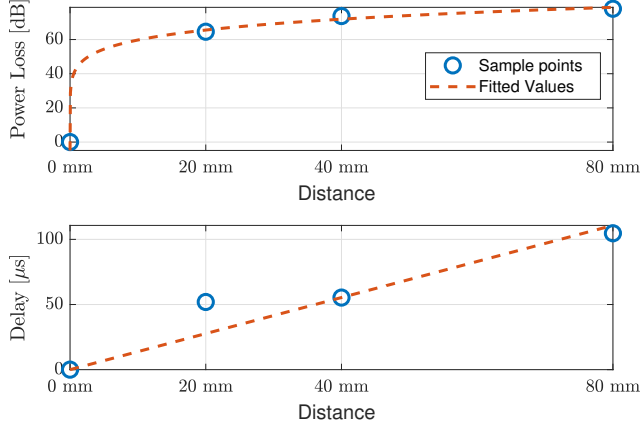


Fig. 6: The curve-fitting results for power loss and delay over distance.

CIR is provided for three specific distances 20, 40, and 80 mm between sender and receiver. Implicitly, the CIR also accounts for the impact of bones and the already included multipath effect.

To be able to compute the gain and delay for distances smaller than 20 mm, we also include the unit gain corresponding to the distance of 0 mm in the curve fitting process. Considering distances smaller than 20 mm allows us to analyze the system's performance for a broader set of monitor locations. We evaluate the gain for each distance as the root mean square (RMS) of the given CIR ( $h_d$ ) yielding

$$g_d = \sqrt{\frac{1}{N} \sum_{k=1}^N h_d^2[k]}, \quad (3)$$

where  $N$  is the length of the sequence and  $h_d[k]$  is the CIR for the given distance  $d'$ , i.e., 20, 40, and 80 mm. For the delay, we compute the mean value (concerning time) plus the standard deviation of the CIR sequences as

$$\tau_{d'} = \bar{\tau}_{d'} + \frac{\tau_{\sigma,d'}}{2}, \quad (4)$$

where

$$\bar{\tau}_{d'} = \frac{1}{f_s} \frac{1}{N} \frac{\sum_{k=1}^N k \cdot h_d^2[k]}{\sum_{k=1}^N h_d^2[k]}, \quad (5)$$

and

$$\tau_{\sigma,d'} = \frac{1}{f_s} \sqrt{\frac{1}{N} \frac{\sum_{k=1}^N (k - f_s \bar{\tau}_{d'})^2 h_d^2[k]}{\sum_{k=1}^N h_d^2[k]}}, \quad (6)$$

where  $f_s$  is the sampling rate of the system. These relations in Equations (5) and (6) evaluate the weighted arithmetic mean, where the weights are defined by the square of the CIR function to neglect its negative values.

Secondly, using the values provided in Equations (3) and (4) for the specific distances, curve fitting is done to provide values for arbitrary distances between nanosensors and the monitor. Among several different results provided by the curve fitting method in Matlab, the one resulting in the least error between the real values and the fitted data is utilized for the gain computation. For fitting a curve to the delay data, we

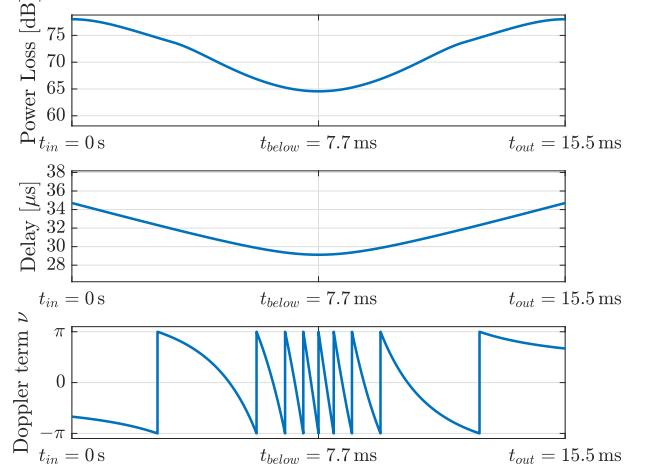


Fig. 7: Results on the perceived loss, delay, and the Doppler term on the travel path when the velocity of the nanosensor is  $v = 0.1$  m/sec and the carrier frequency is  $f_c = 0.4$  MHz

utilize a  $y = a \times x$  line equation due to its linear increase with the distance.

To evaluate the Doppler term, we directly compute the Eq. (2) according to the geometry in Fig. 5. Using trigonometric properties, we compute the angle between the nanosensor and the monitor for each different time-instant  $\phi_t$ . As for the speed, we use the reported blood speeds in arteries ( $v = 0.2$  m/s), capillaries, ( $v = 0.1$  m/s), or veins ( $v = 0.03$  m/s) [28]. For the communication parameters, we use the propagation speed for the ultrasonic waveform as  $c_u = 1480$  m/s, and a center frequency of  $f_c = 1$  MHz.

To illustrate, Fig. 6 depicts the resulting fitted data for the power loss in decibels ( $p_L = -20 \log_{10} g_d$ ), and the delay in the communication range 0–80 mm. Using this curve, we evaluate the resulting gain and delay during the path trajectory of the nanosensor according to its specific distance to the monitor. The resulting evaluation is illustrated in Fig. 7 for the power loss, the delay, and the Doppler term when assuming the traveling speed of 0.1 m/s. As expected, the smallest power loss and delay are obtained when the nanosensor has the shortest distance to the monitor, i.e., for  $t = t_{\text{below}} = 7.7$  ms, which corresponds to the position  $t_{\text{below}}$  in Fig. 5.

According to Fig. 7, the Doppler term (see Eq. (2)) will introduce a remarkable distortion on the received waveform. It will produce a phase shift in the range  $[-\pi, \pi]$  rad along the traveling path. For instance, when considering the transmission of phase shift keying (PSK) waveforms, the impact of movement will severely rotate its constellation points, heavily degrading the communication performance. Analytically, this term introduces a rotation of the constellation coordinates with the angle

$$\Delta\varphi = 2\pi\nu t, \quad (7)$$

according to the exponential term in Eq. (1). The impact of movement on communication performance is discussed

in the next section when integrating this model within the BVS framework.

### B. Implementing the In-Body Communication Link in BVS

BVS is a network simulator ns-3 module, in which the movement of medical nanosensors in a simulated cardiovascular system is implemented, accounting for the impact of the environment on the nanosensors' motion and communication [15]. This module includes all major vessels of the vascular system and enables tracking of the nanosensor' location each second during the simulation. The communication model between the nanosensor and the gateway is implemented as an extension to this BVS module within ns-3.

Communication BVS (C-BVS) consists of three main communication links on top of the conventional BVS module [32]. First of all, the nanosensors must communicate together; thus, it is assumed that they can exchange packets if they are in proximity 1 cm to each other. Moreover, a connection between an external monitor placed on the skin and the nanosensors is required, as aforementioned in the previous sections. Lastly, an end-to-end connection between the monitor and a portable device is also necessary, such that the data collected from the nanosensors is made of use.

Following a similar idea to the channel implementation presented in the previous work in [6], C-BVS enables the implementation of the ultrasonic in-body channel on a macro level. The monitor is located at a fixed position, while the nanosensors are injected at a specified vessel and then travel through the vascular system using the BVS module. Two assumptions are made: on the one hand nanosensor travels from left to right relative to the monitor (see Fig. 5); on the other hand, we assume each time the nanosensor enters a vessel on top of which the monitor is positioned, the nanosensor will definitely travel through the communication range with that monitor.

Following the same steps as in [6], the Doppler term is computed as well as different metrics such as  $\frac{E_b}{N_o}$ , BER, to evaluate the model's performance withing BVS. To evaluate those, the preceding curve fitting and interpolation results for the gain and delay are mapped to the different distances between the external monitor and the nanosensors on every simulation step. The evaluation of BER can give us an insight on the packet delivery ratio (PDR) as well, where PDR is defined as  $(1 - \text{BER})^m$ , such that  $m$  denotes the packet length. Similarly, packet error rate (PER) can be obtained consequently as  $\text{PER} = 1 - (1 - \text{BER})^m$ .

## V. MODELING PAOI

The AoI measures the freshness of the status update about a remote source at the monitoring device. In this research, we target monitoring abnormalities as detected in the HCS. For instance, the information source is the concentration level of QS molecule as sampled by flowing nanosensors in the vessels (see Fig. 1 c). Information flows carried by the nanosensor along the vessels till it is delivered to the monitor device. The monitor device is an external receiver located at the surface of the skin (see Fig. 1 b).

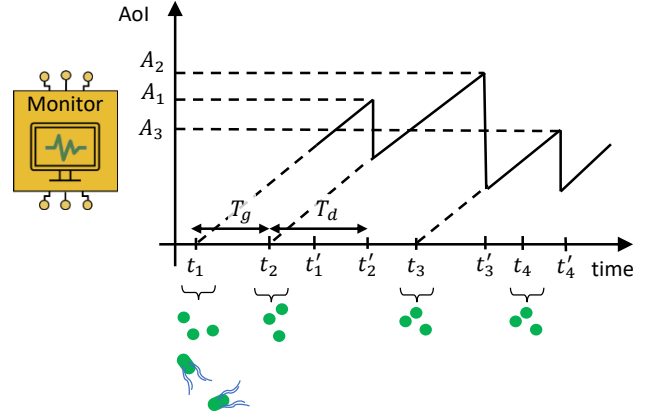


Fig. 8: AoI representation and PAOI values as  $A_1$  to  $A_3$ .

We report the use of the average PAOI metric as an indicator of information aging at the monitor (see [13, Sec. 3.3] concerning the PAOI metric). As depicted in Fig. 8, the peaks  $A_i$ 's are those values just before a new sample arrives at the monitor, which is directly evaluated as the sum of the generation time plus the delay time between the source and the destination (see [33, text below Eq. (8)]). Besides, considering that some packets might get lost, the average PAOI is formulated as [18]

$$\Delta^{(p)} = \frac{1}{1 - p_{\text{loss}}} \mathbf{E}[T_g] + \mathbf{E}[T_d], \quad (8)$$

where  $T_g$  and  $T_d$  denote the generation and delay time intervals, respectively.

The packet-loss event, as characterized by the probability  $p_{\text{loss}}$  in Eq. (8), might happen in two cases. When there are errors in the communication link with the monitor device, as given by the PER, or in case the nanosensor travels twice through the target, which overwrites the current packet. We provide more details to evaluate  $p_{\text{loss}}$  in Section V-C.

The generation time  $T_g$  is produced whenever a nanosensor passes by the target and reads the concentration level of QS molecules. Upon this reading, packets are generated as represented by the time instants  $t_i$  in Fig. 8, where  $T_g = t_i - t_{i-1}$ . We remark that  $T_g$  will be a random variable depending on the traveling nanosensor's path. The generation time will be longer or shorter, depending on the total of nanosensors currently traveling through the target area (more details are given in Section V-A).

Once samples are generated at the target, they travel with the carrier nanosensor to the monitor device and are delivered at the time instant  $t'_i$  (see Fig. 8). The delay  $T_d = t'_i - t_i$ , referred to as the traveling time from the target area to the destination, will generally be a random variable with the outcome dependent on the traveling path from source to destination. See an example in Fig. 2, where the source is the Tibialis Posterior (S42), and the monitor is at the wrist (Capillary Ulnaris in S13).

To evaluate the average generation time and delay in Eq. (8), we rely upon the Markov chain model of the HCS and the corresponding transition probabilities. See a full representation and the corresponding transition probabilities in Fig. 2, as derived in the previous work in [14]. Using the stationary probabilities from the Markov chain, we derive the generation

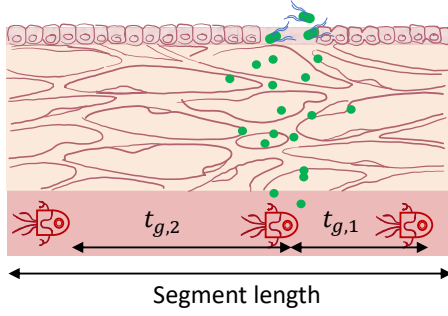


Fig. 9: Visualizing the generation time period as nanosensors flow through the target.

time on the one hand (as explained in Section V-A). On the other hand, we derive the average delay directly using the transition probabilities. Further details on  $T_g$  and  $T_d$  are given below in Sections V-A and V-B, respectively.

#### A. Determining the Average Generation Time

The generation time  $T_g$  refers to the time elapsing between consecutive target samples, which results analogous to finding the time interval between two consecutive nanosensors traveling along the same vessel segment, as represented in Fig. 9 with  $t_{g,1}$  and  $t_{g,2}$ . These time intervals might be modeled according to the exponential distribution, as the sampling event may occur continuously and independently, at a constant average rate  $\lambda$  as (see [34, Sec. 5.5])

$$f_{T_g}(t_g) = \begin{cases} \lambda e^{-\lambda t_g}, & t_g \geq 0, \\ 0 & t_g < 0, \end{cases} \quad (9)$$

where  $\lambda$  refers to the number of nanosensors per unit of time traveling along the vessel  $v$  segment, yielding

$$\lambda_v = \frac{N_v}{T_v}, \quad (10)$$

where  $N_v$  is the total of nanosensors, and  $T_v$  is the traveling time along the vessel segment  $v$ . Thus, the average generation time will be readily given as

$$E[T_g] = \frac{1}{\lambda_v} = \frac{T_v}{N_v}. \quad (11)$$

The traveling time  $T_v$  can be found from physiological parameters like the vessel length and the blood speed, while the total of nanosensors ( $N_v$ ) based with their stationary probability when modeling the HCS with a Markov model (cf. [35]).

To illustrate, let's consider the Tibialis posterior in the legs, where injuries are common. The blood speed in the capillaries is approximately 0.1 m/s [28], and the vessel length is maximum 2 cm around [36], which results in  $T_v \approx 0.2$  s. Besides, in the case of the Tibialis posterior, the probability of finding a single nanosensor is  $p = 0.005$  when looking at the probability for the feet in [14, Fig. 11]. Then, assuming there are a total of  $10^3$  flowing nanosensors in the HCS, approximately  $N_v \approx p \times 10^3 = 5$  nanosensors will be flowing through the Tibialis posterior. Using these approximations, the expected average for the generation time will result in  $E[T_g] \approx \frac{0.2\text{s}}{5} = 40$  ms. A similar procedure applies to evaluate the average generation time for other tissues in the body.

#### B. Determining the Average Delay

Once the packet is generated by sampling physiological variables at the target, it flows with the carrier nanosensor along the vessels. The traveling time from the source to the monitor, denoted as  $T_d$ , will generally be a random variable, depending on the location of the source and the gateway.

To evaluate the average traveling time, we refer to the transition probabilities provided by the Markov model. To illustrate, let's consider the target is in the left Tibialis posterior (referred to as stages S42 in Fig. 2), and the source is attached to the skin close to the heart (referred to stages S1 or S3). Then, the nanosensor will travel with probability one to the heart, and the traveling time will be the sum of the traveling time along each vessel segment from S42 to S1. That is, the traveling time will not be a random variable whenever the monitor is located at the heart, regardless of the location of the source in the capillaries.

However, the traveling time becomes a random variable if the monitor is located on a different vessel segment. To illustrate, let's consider that the monitor is on the left wrist in S13 (like using a smartwatch, the highlighted path in Fig. 2 illustrates this example). Then, a nanosensor with a packet, as generated at the Tibialis Posterior, will travel with probability one to the Arcus Aorta (S5), and with a probability equal to the multiplication of the transition probabilities in the path between S5 and S13 to the wrist. If the nanosensor travels through a different path, the traveling time increases with the path along the corresponding circuit. For instance, if the nanosensor jumps from S5 to the head (S7), it will travel to the heart again to S5, which increases the delay. Then, from there, it might travel or not to the wrist in S13.

Taking this description into account, the average traveling time from S42 to S13 can be evaluated as

$$E[T_d] = T_{S42 \rightarrow S13} \times p_{S42 \rightarrow S13} + \sum_{\substack{c \neq S42 \\ c \neq S13}} \sum_{k=1}^{\infty} (k \times T_c + T_{S42 \rightarrow S13}) \times p_c^k, \quad (12)$$

where  $T_{S42 \rightarrow S13}$  is the traveling time for the direct path between the Tibialis posterior and the wrist (S42 to S13), evaluated as  $p_{S42 \rightarrow S13} = p_{S5 \rightarrow S8} \times p_{S8 \rightarrow S9} \times p_{S9 \rightarrow S10} \times p_{S10 \rightarrow S13}$ . The second term in Eq. (12) accounts for the event (with probability  $p_c^k$ ) that the nanosensor jumps to and travels on different circuits in the body (denoted as  $c$ ) before traveling to the monitor. Each circuit comprises those closed paths between tissues and the heart; consequently, they are uniquely identified with the corresponding tissue label  $c$  and the probability  $p_c$ . The variable  $T_c$  denotes the traveling time along these circuits. Moreover, as we consider the path to the monitor, we also add the term after each circuit that the nanosensor travels along, it will return to the heart (S1) and then travel to the destination (S13). That is why the overall travelling time is the summation of  $k \times T_c$  and  $T_{S42 \rightarrow S13}$ .

The traveling along these circuits  $c$ 's, might happen  $k$  times with probability  $p_c^k$ , thereby the sum in  $k$  and  $c$  in Eq. (12). Besides, the second term does not consider the traveling along the target tissue S42; otherwise the sample will be overwritten

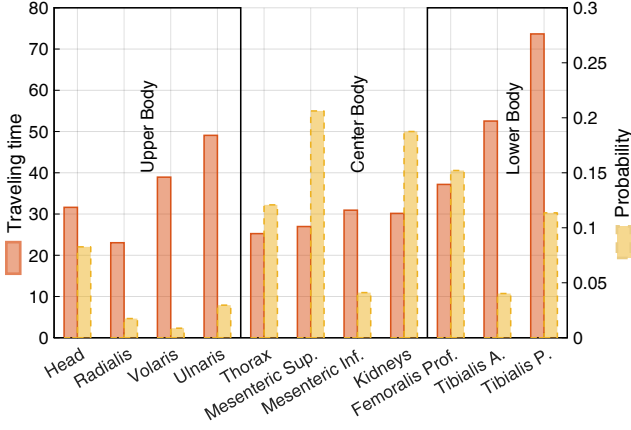


Fig. 10: Average traveling time along the various circuits in the HCS and probabilities per closed loop in the HCS.

and the packet will be lost. That is, the packet will not be delivered at the destination whenever the nanosensor travels two consecutive rounds through the target. The sum does not also consider the circuit with the monitor (S13) otherwise it will evaluate the  $T_d$  twice.

The formula in Eq. (12) can also be written as a closed-form expression after evaluating the sum in  $k$  as

$$E[T_d] = T_{S42 \rightarrow S13} \times p_{S42 \rightarrow S13} + \sum_{\substack{c \neq S42 \\ c \neq S13}} T_c \frac{p_c}{(1-p_c)^2} + T_{S42 \rightarrow S13} \frac{p_c}{1-p_c}, \quad (13)$$

when using the MacLaurin series expansion formulas  $\sum_{k=1}^{\infty} p^k = \frac{p}{1-p}$  and  $\sum_{k=1}^{\infty} k p^k = \frac{p}{(1-p)^2}$ . The remaining sum results finite and can be readily evaluated with  $p_c$ ,  $T_c$  and  $T_{S42 \rightarrow S13}$ .

To determine  $T_c$  in Eq. (5), we use the data provided by BVS concerning the traveling path per nanosensor<sup>2</sup>. From this data, we get the traveling time per tissue which is dependent on the stream the nanosensor is flowing inside the vessels (see [38, Fig. 7]). Averaging along the streams, then we get  $T_c$  as Fig. 10 illustrates.

Finally, to determine the value for  $p_c$  we use the transition probabilities from the Markov model in Fig. 2. To illustrate, in the closed loop comprised of the head and heart,  $p_c$  is evaluated after considering all possibilities for a nanosensor to take this path as  $p_{c, \text{head}} = 0.07 \times 0.27 + 0.03 + 0.05 \times 2 \times 0.56 = 0.0989$ , and a similar evaluation can be done for the other possible closed loops. Applying this procedure to all the Markov model circuits, we get the probabilities illustrated in Fig. 10, where each tissue labels each circuit uniquely.

### C. Determining the Probability for Packet Loss

Once a packet is generated at a given nanosensor, it can get lost for two reasons. The first reason is when the nanosensor travels twice through the same target circuit, and the packet is

<sup>2</sup>We provide open access to the code at [https://github.com/jorge-torresgomez/BVS\\_data](https://github.com/jorge-torresgomez/BVS_data) and also document the BVS's dataset as a datasheet following to Gebru et al. [37].

overwritten. The second case is when the nanosensor travels in the monitor's circuit but the transmission to the monitor device is erroneous, due to the impact of noise and mobility as given by the PER (see Section IV). Having the two cases together the packet loss probability can be evaluated as follows

$$p_{\text{loss}} = \text{PER} \times p_{T \rightarrow M} + p_{T \rightarrow T}, \quad (14)$$

where  $p_{T \rightarrow M}$  denotes the probability of traveling from the target to the monitor without returning to the target, while  $p_{T \rightarrow T}$  denotes the probability of traveling again to the target once the nanosensor flows from there.

We evaluate the probability that the nanosensor travels from the target to the monitor device ( $p_{T \rightarrow M}$ ) with the following reasoning. When the nanosensor collects a sample at the target in the capillaries, it will travel with probability one to the heart, irrespective of the target's location at any capillary in the HCS (see for instance the case at the Tibialis Posterior in Fig. 2). Being at the heart, the nanosensor might travel next to the monitor's circuit with probability  $p_{c=M}$ . The case the nanosensor travels to a different circuit before jumping to the monitor will happen with probability  $p_{c=M} \times (1 - p_{c=T} - p_{c=M})$  (excluding the travel to the target circuit). The case the nanosensor traveled twice along any of the circuits, except for the Target one before visiting the Monitor will happen with probability  $p_{c=M} \times (1 - p_{c=T} - p_{c=M})^2$ . Then, when considering all possible choices, it results in

$$p_{T \rightarrow M} = p_{c=M} \times \sum_{k=0}^{\infty} (1 - p_{c=T} - p_{c=M})^k, \\ = \frac{p_{c=M}}{p_{c=T} + p_{c=M}},$$

after using the MacLaurin series formula  $\sum_{k=0}^{\infty} (1-p)^k = \frac{1}{1-p}$ . Finally, to evaluate  $p_{T \rightarrow T}$ , we follow a similar reasoning yielding

$$p_{T \rightarrow T} = p_{c=T} \times \sum_{k=0}^{\infty} (1 - p_{c=T} - p_{c=M})^k, \quad (15) \\ = \frac{p_{c=T}}{p_{c=T} + p_{c=M}}.$$

## VI. SIMULATION RESULTS

We illustrate the performance of the communication system with the impact of the nanosensor's mobility and the achievable BER and PER in the local link, that is, between nanosensors and the monitor device, on the one hand. On the other hand, we plot the end-to-end average PAoI considering the monitor's at various locations like the heart, wrist and femoralis, while the target is at the Tibialis Posterior. The average PAoI will consider not only the impact of traveling delays but errors in transmissions in the local communication with the monitor device.

### A. Evaluating the Nanosensor-Gateway Communication Link

For local communication between the nanosensor and the monitor device, we assume a propagation speed for the ultrasonic waveform as  $c_u = 1480$  m/s. To illustrate, we performed simulations in which we transmitted a binary phase

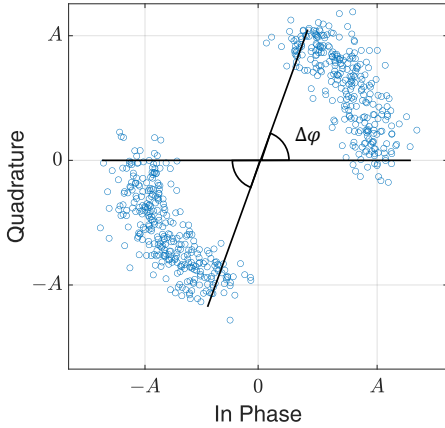


Fig. 11: Recovered constellation points for a nanosensor traveling speed of 0.03 m/sec, SNR = 15 dB, and a center frequency  $f_c = 1$  MHz.

shift keying (BPSK) waveform, as indicated in [7], with a transmission rate of 10 kbit/s and of amplitude  $A = 1$ . For transmissions, we assume a center frequency as  $f_c = 0.4$  MHz as it results in less attenuation with time (see [6, Figures 6 and 8]). Furthermore, we assumed the additive white gaussian noise (AWGN) model (as given in [7]) to evaluate the impact of noise in the channel. We assume a noise spectral density as  $N_o = -107$  dB/Hz to evaluate SNR = 15 dB at the communication distance  $d = 80$  mm.

Fig. 11 visualizes the impact of mobility on the recovered constellation points, where the nanosensor velocity is 0.03 m/s as the blood in the veins. The transmission starts while the nanosensor is at the position provided by  $t_{in} = 0$  ms (see Fig. 3); corresponding to the largest distance to the monitor as  $d = 80$  mm and SNR = 15 dB. Although constant noise level produces spreading, the impact of mobility is clearly visible in the rotation of the constellation points, represented by the angle  $\Delta\varphi$  as in Eq. (7).

As a result, the emitted coordinates  $(-A, 0)$  and  $(A, 0)$  are rotated over time to  $(0, -A)$  and  $(0, A)$ , respectively. This is produced by the dominating Doppler factor  $\nu$  as depicted in Fig. 7 c) and according to Eq. (2). The rotation of the constellation will consequently produce a severe degradation of the BER when decoding the received BPSK waveform.

In our previous work, the impact of mobility on the communication performance was evaluated by simulating the channel model as given in Eq. (1) in Matlab [6]. Based on this model, we presented results regarding BER and  $\frac{E_b}{N_o}$ , focusing on the impact that different parameters, such as used frequency and nanosensor's speed have on the performance of a mobility-based system. This work evaluates the BER performance by implementing the ultrasonic in-body-to-body area network connection on ns-3 to study large-scale effects. Similarly, in the ns-3 environment, a BPSK waveform is emitted when the nanosensor is in communication range with the external monitor. The simulation results evaluate the impact of the monitor's location, where four different tissues are considered: the heart, the femoralis, the left wrist, and the left ankle.

For a fair evaluation of the BER and PER, among these four

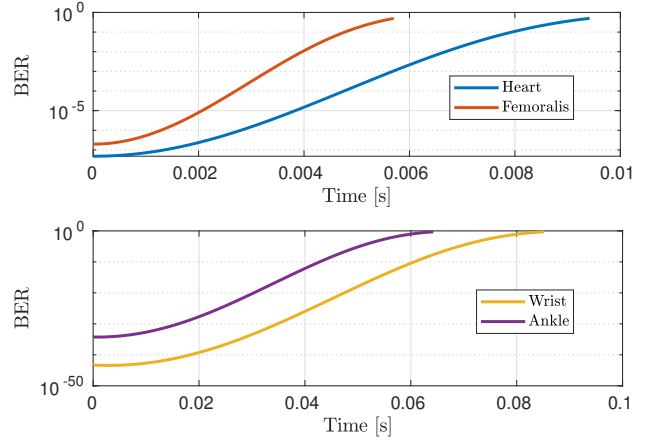


Fig. 12: Achievable BER versus time for different locations of the external monitor (heart, femoralis, wrist, and ankle). The velocity of the nanosensor is 0.2 m/sec for the heart, and 0.1 m/sec for the other cases.

scenarios, we refer to the illustration in Fig. 4 for computing the minimum communication distance between the monitor and the nanosensor and the maximum possible communication distance between them. The minimum distances for these four different monitor positions are 20 mm, 32.8 mm, 2 mm, and 2.8 mm for the heart, femoralis, wrist and ankle, respectively.

The angle  $\varphi$  in Fig. 4 is assumed to be  $30^\circ$ , and by using the Pythagoras theorem, the maximum possible communication distance is computed. As for the nanosensor velocity,  $v = 0.2$  m/s is assumed for the cases of the heart and the femoralis, whereas  $v = 0.1$  m/s for the wrist and the ankle. The BER values are obtained for each case until it degrades to 0.5 units.

The results for the BER are plotted in Fig. 12. When the monitor is located at heart, the BER degrades slower than when it is located at the femoralis, because the path loss is lower for the former case. Similar behavior is obtained when comparing the case of the monitor located at the wrist to when it is located at the ankle. The impact of the velocity can be observed as well, given that a better overall BER performance is obtained when the velocity of the nanosensors is smaller. We remark that the BER results in the order of  $10^{-50}$  at  $t$  around zero due to the shorter distance between the vessel and the skin in the wrist and the ankle. Although the noise level remains the same, the attenuation is highly reduced.

Secondly, the impact of the location of the external monitor on the PER is investigated. Packets of 8-bits length are considered, in this way, the PER is computed as  $PER = 1 - (1 - BER)^8$ . A similar behavior to that of Fig. 12 can be seen on Fig. 13 as well, where the delivery ratio drops faster when the path loss is higher and when the velocity (hence Doppler effect) is higher as well.

### B. Evaluating the Average PAoI at the Monitor Device

We evaluate the average PAoI with Eq. (8) when using Eq. (11) to evaluate the average generation time, Eq. (13) to evaluate the packet delay, and Eq. (14) to evaluate  $p_{loss}$ . Although the expression in Eq. (13) targets the delay between

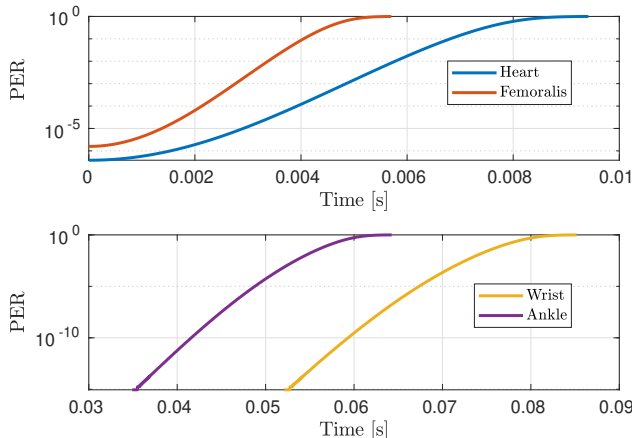


Fig. 13: Achievable PER versus time for different locations of the external monitor (heart, femoralis, wrist, and ankle). The velocity of the nanosensor is 0.2 m/sec for the heart, and 0.1 m/sec for the other cases. The packet length is assumed to be 8 bits.

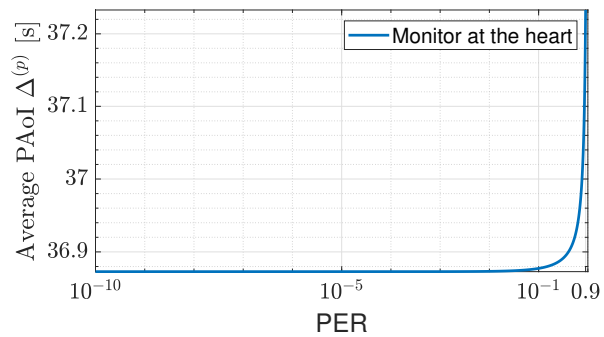
the Tibialis Posterior (S42) and the left wrist (S13), it also states for other link pairs when replacing the indexes accordingly. We target the source at the Tibialis Posterior and analyze the perceived average PAoI with the monitor located at three positions on the skin's surface: heart, left wrist, and left Femoralis Profundis (see Fig. 2).

Following the example in Section V-A, the average generation time at the Femoralis Posterior approximately results in  $E[T_g] \approx 40$  ms when the total of flowing nanosensors is  $10^3$ . Meanwhile, the average delay will be deterministic when the monitor device is at the heart; after passing by any capillary system, all the nanosensors flow to the heart. In this case, the average delay results in  $E[T_d] \approx 40$  ms as reported by the BVS framework. If the monitor is placed at a different location (wrists or femoris), then we use Eq. (13).

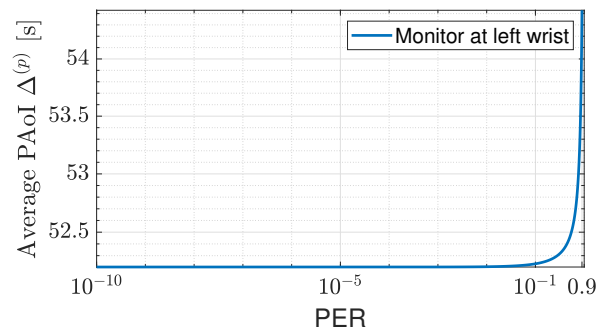
Fig. 14 depicts the average PAoI for the various monitor's locations with the PER. All the cases exhibit a monotonic increase as the PER increases. However, the impact of local communication becomes relevant only when the PER is close to one. That is, the average PAoI remains almost constant, in the scale of seconds when the PER is less than  $10^{-1}$  units. Besides, the information age accounts for the less when the monitor is at heart ( $\approx 36$  s) and becomes larger when located at the wrist ( $\approx 48.6$  s) or the Femoralis ( $\approx 48.5$  s). These results agree with the certain to travel to the heart once leaving the target, and with the higher probability to travel to the Femoralis Profundis than to the Wrist (Capillaris Ulnaris in Fig. 10).

## VII. CONCLUSION

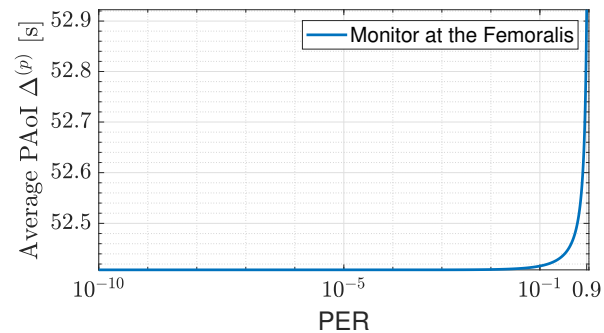
In this paper, we evaluate the timely detection of the information gathered by the flowing nanosensors in the HCS to external monitoring devices. We report a methodology to compute the average PAoI metric, which accounts for the information freshness. In evaluating this metric, we integrated the random mobility of nanosensors while flowing in the HCS and the impact of the channel in the communication



(a) Heart



(b) Left wrist



(c) Femoralis Profundis

Fig. 14: Average PAoI when the gateway is located at the heart, the left wrist, and the Femoralis Profundis. The target is referred to as the Tibialis Posterior. Please note the different scale of the y-axis.

link between nanosensors and the monitor device. Extending previous results, we further evaluate the performance of the ultrasonic communication channel through its implementation in the network simulator ns-3 in combination with BVS. The results show the importance of the location of the external monitor on the human body and its impact on the BER, the PER, and the average PAoI. Surprisingly, the resulting average PAoI metric is independent of the PER. We observe little variability of the average PAoI in the order of seconds when PER is less than  $10^{-1}$ .

The large-scale simulation on ns-3 and the inclusion of the PAoI metric for evaluation open the path for new research on protocol design for ultrasonic communication in-body-to-body area networks connection. Moreover, including non-constant velocities for the nanosensors, considering that the bloodstream transports them, can be considered in future works.

## REFERENCES

- [1] I. F. Akyildiz, F. Brunetti, and C. Blázquez, “Nanonetworks: A New Communication Paradigm,” *Elsevier Computer Networks (COMNET)*, vol. 52, pp. 2260–2279, 2008.
- [2] L. Felicetti, M. Femminella, G. Reali, and P. Liò, “A Molecular Communication System in Blood Vessels for Tumor Detection,” in *1st ACM International Conference on Nanoscale Computing and Communication (NANOCOM 2014)*, Atlanta, GA: ACM, May 2014.
- [3] F. Dressler and S. Fischer, “Connecting In-Body Nano Communication with Body Area Networks: Challenges and Opportunities of the Internet of Nano Things,” *Elsevier Nano Communication Networks*, vol. 6, pp. 29–38, Jun. 2015.
- [4] Q. H. Abbasi, K. Yang, N. Chopra, et al., “Nano-Communication for Biomedical Applications: A Review on the State-of-the-Art From Physical Layers to Novel Networking Concepts,” *IEEE Access*, vol. 4, pp. 3920–3935, Oct. 2016.
- [5] I. F. Akyildiz and J. M. Jornet, “The Internet of Nano-Things,” *IEEE Wireless Communications*, vol. 17, no. 6, pp. 58–63, Dec. 2010.
- [6] J. Torres Gómez, A. Kuestner, L. Stratmann, and F. Dressler, “Modeling Ultrasonic Channels with Mobility for Gateway to In-Body Nanocommunication,” in *IEEE Global Telecommunications Conference (GLOBECOM 2022)*, Rio de Janeiro, Brazil: IEEE, Dec. 2022, pp. 4535–4540.
- [7] T. Bos, W. Jiang, J. D’hooge, M. Verhelst, and W. Dehaene, “Enabling Ultrasound In-Body Communication: FIR Channel Models and QAM Experiments,” *IEEE Transactions on Biomedical Circuits and Systems*, pp. 135–144, Feb. 2019.
- [8] E. C. Sciacca and L. Galluccio, “Impulse response analysis of an ultrasonic human body channel,” *Elsevier Computer Networks (COMNET)*, vol. 171, p. 107149, Apr. 2020.
- [9] L. Galluccio, T. Melodia, S. Palazzo, and G. E. Santagati, “Challenges and Implications of Using Ultrasonic Communications in Intra-body Area Networks,” in *9th IEEE/IFIP Conference on Wireless On demand Network Systems and Services (WONS 2012)*, Courmayeur, Italy: IEEE, Jan. 2012, pp. 182–189.
- [10] T. Hogg and R. A. Freitas Jr., “Acoustic communication for medical nanorobots,” *Elsevier Nano Communication Networks*, vol. 3, no. 2, pp. 83–102, Jun. 2012.
- [11] B. Jaafar, J. A. Neasham, and P. Degenaar, “What is Ultrasound Can and Cannot Do in The Communication of Biomedical Implanted Medical Devices,” *IEEE Reviews in Biomedical Engineering*, vol. 16, pp. 357–370, May 2021.
- [12] G. E. Santagati, N. Dave, and T. Melodia, “Design and Performance Evaluation of an Implantable Ultrasonic Networking Platform for the Internet of Medical Things,” *IEEE/ACM Transactions on Networking (TON)*, vol. 28, no. 1, pp. 29–42, 2020.
- [13] A. Kosta, N. Pappas, and V. Angelakis, “Age of Information: A New Concept, Metric, and Tool,” *Foundations and Trends® in Networking*, vol. 12, no. 3, pp. 162–259, Nov. 2017.
- [14] J. Torres Gómez, J. L. González Rios, and F. Dressler, “Nanosensor Location in the Human Circulatory System based on Electric Circuit Representation of Vessels,” in *9th ACM International Conference on Nanoscale Computing and Communication (NANOCOM 2022)*, Barcelona, Spain: ACM, Oct. 2022, pp. 1–7.
- [15] R. Geyer, M. Stelzner, F. Büther, and S. Ebers, “BloodVoyagerS: Simulation of the Work Environment of Medical Nanobots,” in *5th ACM International Conference on Nanoscale Computing and Communication (NANOCOM 2018)*, Reykjavik, Iceland: ACM, Sep. 2018, 5:1–5:6.
- [16] B. Atakan, O. B. Akan, and S. Balasubramaniam, “Body Area NanoNetworks with Molecular Communications in Nanomedicine,” *IEEE Communications Magazine (COMMAG)*, vol. 50, no. 1, pp. 28–34, Jan. 2012.
- [17] N. Farsad, H. B. Yilmaz, A. W. Eckford, C.-B. Chae, and W. Guo, “A Comprehensive Survey of Recent Advancements in Molecular Communication,” *IEEE Communications Surveys & Tutorials*, vol. 18, no. 3, pp. 1887–1919, 2016.
- [18] J. Torres Gómez, K. Pitke, L. Stratmann, and F. Dressler, “Age of Information in Molecular Communication Channels,” *Elsevier Digital Signal Processing (DSP), Special Issue on Molecular Communication*, vol. 124, p. 103108, May 2022.
- [19] J. M. Jornet and I. F. Akyildiz, “Channel Modeling and Capacity Analysis for Electromagnetic Wireless Nanonetworks in the Terahertz Band,” *IEEE Transactions on Wireless Communications (TWC)*, vol. 10, no. 10, pp. 3211–3221, Oct. 2011.
- [20] P. Wang, J. M. Jornet, M. A. Malik, N. Akkari, and I. F. Akyildiz, “Energy and spectrum-aware MAC protocol for perpetual wireless nanosensor networks in the Terahertz Band,” *Elsevier Ad Hoc Networks*, vol. 11, no. 8, pp. 2541–2555, Nov. 2013.
- [21] J. M. Jornet and I. F. Akyildiz, “Graphene-based Plasmonic Nano-Antenna for Terahertz Band Communication in Nanonetworks,” *IEEE Journal on Selected Areas in Communications (JSAC)*, vol. 31, no. 12, pp. 685–694, Dec. 2013.
- [22] G. E. Santagati, T. Melodia, L. Galluccio, and S. Palazzo, “Medium Access Control and Rate Adaptation for Ultrasonic Intra-body Sensor Networks,” *IEEE/ACM Transactions on Networking (TON)*, vol. 23, no. 4, pp. 1121–1134, Aug. 2015.
- [23] A. Kuestner, K. Pitke, J. Torres Gómez, R. Wendt, S. Fischer, and F. Dressler, “Age of Information in In-Body Nano Communication Networks,” in *8th ACM International Conference on Nanoscale Computing and Communication (NANOCOM 2021)*, Virtual Conference: ACM, Sep. 2021, 27:1–27:2.
- [24] R. Smith, A. Arca, X. Chen, et al., “Design and fabrication of ultrasonic transducers with nanoscale dimensions,” *Journal of Physics: Conference Series*, vol. 278, p. 012035, Jan. 2011.
- [25] Y. Davilis, A. Kalis, and A. Ifantis, “On the Use of Ultrasonic Waves as a Communications Medium in Biosensor Networks,” *IEEE Transactions on Information Technology in Biomedicine*, vol. 14, no. 3, pp. 650–656, May 2010.
- [26] C. Gatsonis, J. S. Hodges, R. E. Kaas, and N. D. Singpurwalla, *Case Studies in Bayesian Statistics*. Springer Science & Business Media, 2012, vol. II.
- [27] J. Torres Gómez, R. Wendt, A. Kuestner, K. Pitke, L. Stratmann, and F. Dressler, “Markov Model for the Flow of Nanobots in the Human Circulatory System,” in *8th ACM International Conference on Nanoscale Computing and Communication (NANOCOM 2021)*, Virtual Conference: ACM, Sep. 2021, 5:1–5:7.
- [28] A. C. Guyton and M. E. Hall, *Guyton and Hall Textbook of Medical Physiology*, 14th ed. Elsevier, 2015.
- [29] P. Oltulu, B. Ince, N. Kokbudak, S. Findik, and F. Kilinc, “Measurement of epidermis, dermis, and total skin thicknesses from six different body regions with a new ethical histometric technique,” *Turkish Journal of Plastic Surgery*, vol. 26, no. 2, p. 56, 2018.
- [30] G. Piro, P. Bia, G. Boggia, D. Caratelli, L. A. Grieco, and L. Mescia, “Terahertz electromagnetic field propagation in human tissues: A study on communication capabilities,” *Nano Communication Networks*, vol. 10, pp. 51–59, Dec. 2016.
- [31] G. Matz and F. Hlawatsch, “Fundamentals of Time-Varying Communication Channels,” in *Wireless Communications Over Rapidly Time-Varying Channels*, F. Hlawatsch and G. Matz, Eds., Elsevier, 2011, pp. 1–63.
- [32] A. Kuestner, L. Stratmann, R. Wendt, S. Fischer, and F. Dressler, “A Simulation Framework for Connecting In-Body Nano Communication with Out-of-Body Devices,” in *7th ACM International Conference on Nanoscale Computing and Communication (NANOCOM 2020)*, Virtual Conference: ACM, Sep. 2020.
- [33] R. D. Yates, Y. Sun, D. R. Brown III, S. K. Kaul, E. Modiano, and S. Ulukus, “Age of Information: An Introduction and Survey,” *IEEE Journal on Selected Areas in Communications (JSAC)*, vol. 39, no. 5, pp. 1183–1210, May 2021.
- [34] S. Ross, *A First Course in Probability*, 8th ed. Upper Saddle River, NJ: Prentice Hall, 2010, p. 545.
- [35] J. Torres Gómez, A. Kuestner, J. Simonjan, B. D. Unluturk, and F. Dressler, “Nanosensor Location Estimation in the Human Circulatory System using Machine Learning,” *IEEE Transactions on Nanotechnology (TNANO)*, vol. 21, pp. 663–673, Oct. 2022.
- [36] C. J. Salgado, S. L. Moran, S. Mardini, and F.-C. Wei, “Fibula flap,” in *Flaps and Reconstructive Surgery*, F.-C. Wei and S. Mardini, Eds., Elsevier, 2009, pp. 441–457.
- [37] K. Gebru, J. Morgenstern, B. Vecchione, et al., “Datasheets for datasets,” *Communications of the ACM*, vol. 64, no. 12, pp. 86–92, Dec. 2021.
- [38] J. Torres Gómez, A. Kuestner, K. Pitke, J. Simonjan, B. D. Unluturk, and F. Dressler, “A Machine Learning Approach for Abnormality Detection in Blood Vessels via Mobile Nanosensors,” in *19th ACM Conference on Embedded Networked Sensor Systems (SenSys 2021), 2nd ACM International Workshop on Nanoscale Computing, Communication, and Applications (NanoCoCoA 2021)*, Coimbra, Portugal: ACM, Nov. 2021, pp. 596–602.